

Supporting Information

© Wiley-VCH 2011

69451 Weinheim, Germany

Porous and Dense Magnesium Borohydride Frameworks: Synthesis, Stability, and Reversible Absorption of Guest Species**

Yaroslav Filinchuk, Bo Richter, Torben R. Jensen,* Vladimir Dmitriev, Dmitry Chernyshov, and Hans Hagemann*

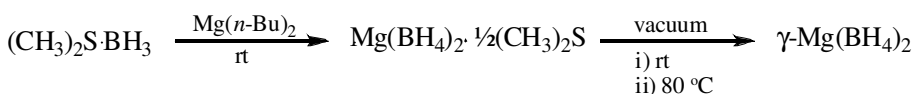
anie_201100675_sm_miscellaneous_information.pdf

Supporting information

Contents:

1. Synthesis of $\text{Mg}(\text{BH}_4)_2 \cdot \frac{1}{2}\text{S}(\text{CH}_3)_2$ intermediate and the nanoporous cubic $\gamma\text{-Mg}(\text{BH}_4)_2$
2. Diffraction experiments at ambient conditions
3. Structure solution and refinement for $\text{Mg}(\text{BH}_4)_2 \cdot \frac{1}{2}\text{S}(\text{CH}_3)_2$
4. Structure solution and refinement for the cubic $\gamma\text{-Mg}(\text{BH}_4)_2$
5. Absorption-desorption of organic guest molecules in the porous $\gamma\text{-Mg}(\text{BH}_4)_2$
6. Localization of dichloromethane in the porous $\gamma\text{-Mg}(\text{BH}_4)_2$
7. Absorption-desorption of N_2 and H_2 gases in the porous $\gamma\text{-Mg}(\text{BH}_4)_2$
8. Localization of the gas molecules in the porous $\gamma\text{-Mg}(\text{BH}_4)_2$
9. Desorption isobars for N_2 and H_2 in the porous $\gamma\text{-Mg}(\text{BH}_4)_2$ determined from *in-situ* synchrotron radiation powder X-ray diffraction data
10. High-pressure (HP) diffraction experiments
11. Structure solution and refinement for the HP tetragonal $\delta\text{-Mg}(\text{BH}_4)_2$
12. Pressure-induced phase transitions in α -, γ - and $\delta\text{-Mg}(\text{BH}_4)_2$
13. Equations of state and volume collapses for α -, γ - and $\delta\text{-Mg}(\text{BH}_4)_2$
14. Pressure and temperature evolution of $\delta\text{-Mg}(\text{BH}_4)_2$
15. Geometry of MgH_8 polyhedra in the experimental and the most stable theoretically predicted $\text{Mg}(\text{BH}_4)_2$ structures
16. Characterization of $\gamma\text{-Mg}(\text{BH}_4)_2$ surface area and pore size by physisorption of nitrogen
17. Calculation of surface area and pore volume and size in $\gamma\text{-Mg}(\text{BH}_4)_2$ from the crystal structure
18. Determination of isosteric heats of N_2 and H_2 adsorption in $\gamma\text{-Mg}(\text{BH}_4)_2$, using *in-situ* diffraction data collected through a set of isobars
19. Comparison of IR and Raman spectra for the amorphous and crystalline $\text{Mg}(\text{BH}_4)_2$
20. References

1. Synthesis of $\text{Mg}(\text{BH}_4)_2 \cdot \frac{1}{2}\text{S}(\text{CH}_3)_2$ intermediate and the nanoporous cubic $\gamma\text{-Mg}(\text{BH}_4)_2$.



To a stirred solution of $(\text{CH}_3)_2\text{S}\cdot\text{BH}_3$ (2M in toluene, 18.0 mL, 36.0 mmol), $\text{Mg}(n\text{-Bu})_2$ was added (1 M solution in heptanes, 10 mL, 10.0 mmol) at room temperature and under inert atmosphere. Adding was done dropwise and slowly, carefully monitoring exothermic reaction. After stirring at room temperature for 2 h, the reaction mixture was filtered using a Schlenk filtration apparatus and subsequently washed with toluene (anhydrous, 3x10 mL). The solvated product $\text{Mg}(\text{BH}_4)_2 \cdot \frac{1}{2}\text{S}(\text{CH}_3)_2$ was obtained as a white crystalline solid, collected and dried for 12-16 h at room temperature on a vacuum line ($2 \cdot 10^{-2}$ mbar). Yield of $\text{Mg}(\text{BH}_4)_2 \cdot \frac{1}{2}\text{S}(\text{CH}_3)_2$ 0.596 g (70%). $\gamma\text{-Mg}(\text{BH}_4)_2$ was obtained by constant heating of $\text{Mg}(\text{BH}_4)_2 \cdot \frac{1}{2}\text{S}(\text{CH}_3)_2$ at 80°C on a vacuum line ($2 \cdot 10^{-2}$ mbar) for 12-16 h. Yield of $\gamma\text{-Mg}(\text{BH}_4)_2$ 0.370 g (68.5%).

2. Diffraction experiments at ambient conditions. Synchrotron radiation powder X-ray diffraction (SR-PXD) data were collected at the Swiss-Norwegian beamline BM1A at the European Synchrotron Radiation Facility (ESRF) (Grenoble, France) using a MAR345 image plate detector. The wavelength used in different experiments ranged from 0.70 to 0.75 \AA , and the sample-to-detector distance ranged from 150 to 400 mm. These parameters along with image plate tilt angles were calibrated using a standard LaB_6 sample. Samples were enclosed under argon into thin-walled glass capillaries. The two-dimensional diffraction images were azimuthally integrated using the ESRF Fit2D program^{S1}.

3. Structure solution and refinement for $\text{Mg}(\text{BH}_4)_2 \cdot \frac{1}{2}\text{S}(\text{CH}_3)_2$. 13 diffraction peaks were indexed by DICVOL2004^{S2} in a centered monoclinic cell. Analysis of systematic absences suggested space groups $C2/c$ and Cc . The structure was solved in Cc by global optimization in direct space by program FOX^{S3}. Positions of two Mg atoms, and position and orientation of one organic molecule and four borohydride groups were optimized, applying rigid body and antibump restraints. Bond distances and angles for the dimethylsulfide were approximated by those of the free molecule optimized in the program HyperChem, Release 6.0 (Hypercube Inc., Gainesville, Florida, USA). Examination of the resulting structure and analysis by Platon^{S4} did not find a higher crystallographic symmetry. The search for solvent accessible volume identified only one very small void of 16 \AA^3 (at $x = 0.138$, $y = 0.313$, $z = 0.412$), thus showing that the structure cannot host any guest molecules and is not porous.

The final refinement was done in Cc by the Rietveld method using program Fullprof^{S5}. 40 distance restraints for interatomic distances and 37 for angles were used and 14 wt% of the secondary phase, the

cubic γ -Mg(BH₄)₂ (see below) was also modelled. The background was described by linear interpolation between selected points. The final discrepancy factors are: $R_B = 3.9\%$, $R_F = 5.9\%$, $R_p = 6.3\%$, and $R_{wp} = 7.0\%$. The refinement profile is shown in Fig. S1. Crystal data and atomic coordinates are listed in Table S1.

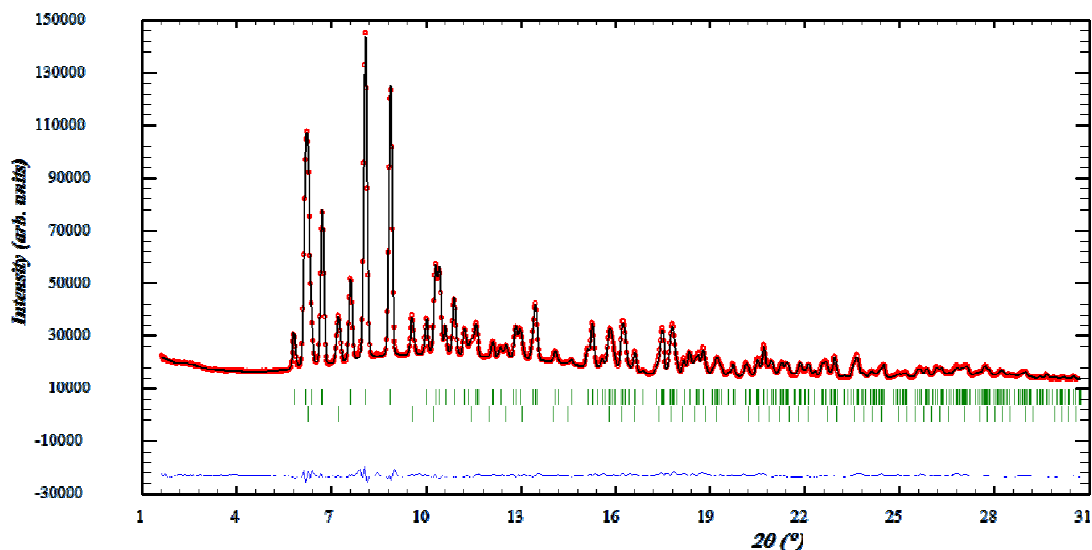


Figure S1. Rietveld refinement profile for Mg(BH₄)₂· $\frac{1}{2}$ S(CH₃)₂. The green marks show Bragg positions, the second row of marks corresponds to 14 wt% of γ -Mg(BH₄)₂ ($\lambda = 0.703511$ Å).

Table S1. Experimental structural parameters for Mg(BH₄)₂· $\frac{1}{2}$ S(CH₃)₂ at ambient conditions. Space group Cc , $Z = 4$, $a = 7.6325(4)$, $b = 13.8411(8)$, $c = 12.4290(8)$ Å, $\beta = 103.833(3)^\circ$, $V = 1274.94(13)$ Å³. All atoms fully occupy general positions.

Atom	x	y	z
Mg1	0.4764(12)	0.0884(5)	0.5521(7)
Mg2	0.0392(12)	0.7344(4)	0.2017(8)
S	0.1925(10)	0.0071(4)	0.4141(7)
C1	0.0416(12)	0.1022(6)	0.3481(9)
C2	0.0552(12)	-0.0501(7)	0.4952(8)
H1	0.0118(12)	0.1444(6)	0.4015(9)
H2	-0.0647(12)	0.0722(6)	0.3040(9)
H3	0.1040(12)	0.1367(6)	0.3009(9)
H4	-0.0181(12)	-0.0067(7)	0.5265(8)

H5	0.1407(12)	-0.0805(7)	0.5546(8)
H6	-0.0202(12)	-0.0973(7)	0.4487(8)
B1	0.5359(6)	0.1602(3)	0.3798(4)
H11	0.588(10)	0.086(3)	0.413(5)
H12	0.483(11)	0.203(3)	0.444(4)
H13	0.651(6)	0.203(6)	0.359(4)
H14	0.421(7)	0.151(7)	0.303(3)
B2	0.7689(6)	0.8410(3)	0.1741(4)
H21	0.894(6)	0.851(5)	0.244(5)
H22	0.644(5)	0.850(6)	0.209(4)
H23	0.767(6)	0.898(5)	0.107(6)
H24	0.768(7)	0.766(3)	0.137(7)
B3	0.5565(6)	0.0860(3)	0.1063(4)
H31	0.604(10)	0.046(3)	0.038(5)
H32	0.463(10)	0.147(3)	0.066(4)
H33	0.481(10)	0.035(3)	0.151(5)
H34	0.680(5)	0.115(4)	0.168(6)
B4	0.2731(6)	0.8330(3)	0.1500(3)
H41	0.284(8)	0.801(7)	0.236(3)
H42	0.305(10)	0.9134(14)	0.160(6)
H43	0.372(8)	0.794(3)	0.110(6)
H44	0.132(4)	0.823(6)	0.095(4)

4. Structure solution and refinement for the cubic γ -Mg(BH₄)₂. A powder pattern of a single-phase sample was indexed in EXPO2009^{S6}. The space group was determined to be *Id-3a* based on the unit cell dimensions and systematic absences observed. The crystal structure was solved by parallel tempering in FOX^{S3}, using one Mg atom and position and orientation of one rigid (B-H 1.22 Å) borohydride group.

Antibump restraints of 2 Å were used for Mg-H and of 2.5 Å for H...H distances. The model was refined by Fullprof^{S5}, keeping the orientation of the BH₄ group fixed. Besides the cell and profile parameters, only two coordinates for the BH₄ group and two atomic displacements for Mg atom and the BH₄ group were refined. The background was described by linear interpolation between selected points. The final discrepancy factors are: $R_B = 4.4\%$, $R_F = 6.2\%$, $R_p = 11.1\%$, and $R_{wp} = 8.8\%$. The refinement profile is shown in Fig. S2. Crystal data and atomic coordinates are listed in Table S2.

A probe with a radius of 1.2 Å, similar to the van der Waals radius of a hydrogen atom, was used to identify empty voids by the program Platon^{S4}. An infinite 3D porosity in γ -Mg(BH₄)₂ was detected, corresponding to 33 % of the structure volume. Rietveld refinements showed that the cavities in γ -Mg(BH₄)₂ are unoccupied.

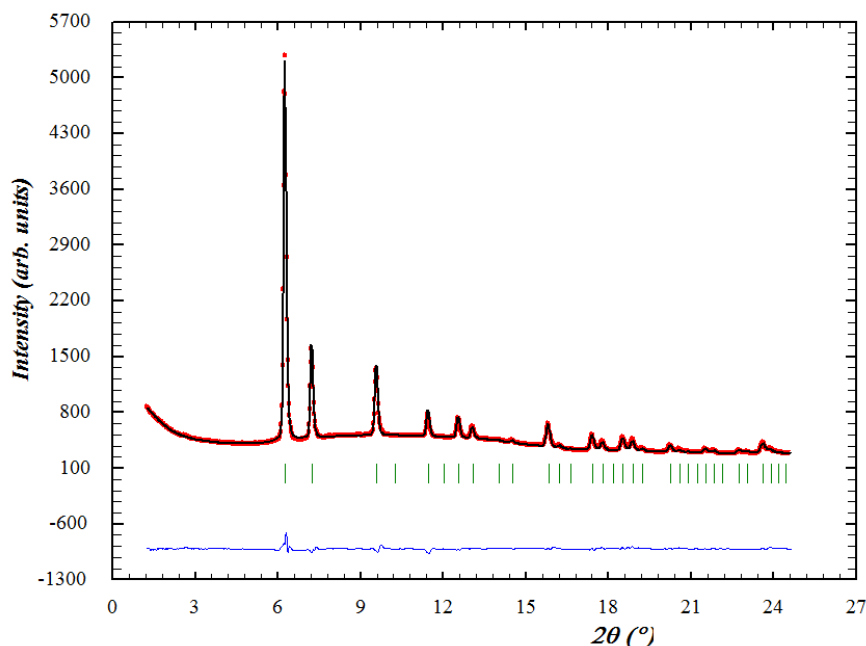


Figure S2. Rietveld refinement profile for γ -Mg(BH₄)₂. The green marks show Bragg positions ($\lambda = 0.703511$ Å).

Table S2. Experimental structural parameters for the cubic structure of γ -Mg(BH₄)₂ at ambient conditions. Space group $Ia-3d$, $Z = 24$, $a = 15.7575(16)$ Å, $V = 3912.6(7)$ Å³.

Atom	Wyckoff site	x	y	z
Mg	24d	1/4	1/8	1/2

B	48g	0.3098(2)	0.0598(2)	3/8
H1	96h	0.2857(2)	0.0207(2)	0.4373
H2	96h	0.2974(2)	0.1355(2)	0.3856

5. Absorption-desorption of organic guest molecules in the porous γ -Mg(BH₄)₂. Six aprotic solvents were tested for insertion into the porous structure: hexane, toluene, dimethylformamide, dimethylsulfoxide, chloroform and dichloromethane. A powdered sample of nanoporous γ -Mg(BH₄)₂ was enclosed in a glass capillary, wetted by a solvent and simultaneously exposed to synchrotron X-rays. Powder X-ray diffraction data revealed that only dichloromethane is hosted inside the pores. Thermodesorption experiments (using a Oxford Cryostream 700+ temperature controller) monitored *in-situ* by SR-PXD revealed release of the guest molecule at 313-322 K, with a full recovery of the porous cubic γ -Mg(BH₄)₂. Thus, the guest insertion is reversible, and its departure is fast and complete.

6. Localization of dichloromethane in the porous γ -Mg(BH₄)₂. Guest molecule localization was determined using the SR-PXD data and global optimization in direct space by FOX^{S3}. The structure of the porous γ -Mg(BH₄)₂ framework was fixed, and the position, orientation and occupancy of the organic molecule were optimized. Antibump restraints of 2 Å were used for Mg...Cl, H...H contacts and of 2.5 Å for H...Cl distances. The resulting model was refined by Fullprof^{S5}, varying profile and cell parameters, occupancy and group atomic displacement for the guest molecule. The refined composition of the host-guest structure is Mg(BH₄)₂·0.18CH₂Cl₂. The background was described by linear interpolation between selected points. The final discrepancy factors are: $R_B = 4.4\%$, $R_F = 6.2\%$, $R_p = 11.1\%$, and $R_{wp} = 8.8\%$. The refinement profile is shown in Fig. S3. Crystal data and atomic coordinates are listed in Table S3. The crystal structure of the guest-host material is shown in Figure S4.

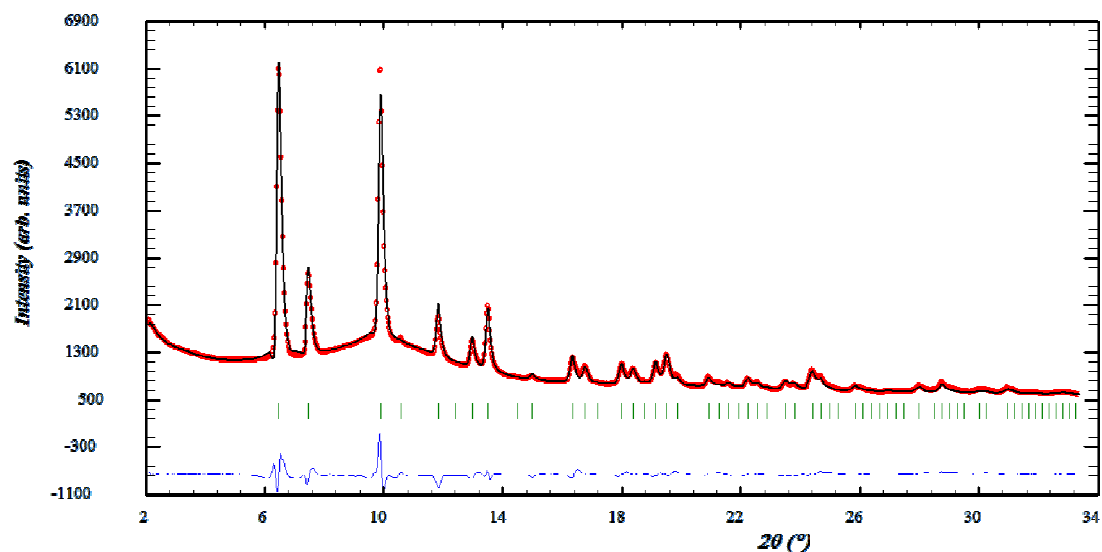


Figure S3. Rietveld refinement profile for γ -Mg(BH₄)₂·0.18CH₂Cl₂. The green marks show Bragg positions ($\lambda = 0.730650 \text{ \AA}$).

Table S3. Experimental structural parameters for γ -Mg(BH₄)₂·0.18CH₂Cl₂ at ambient conditions. Space group *Ia-3d*, $Z = 24$, $a = 15.844(3) \text{ \AA}$, $V = 3977.2(12) \text{ \AA}^3$.

Atom	Wyckoff site	x	y	z	Occupancy
Mg	24d	1/4	1/8	1/2	1
B	48g	0.3098	0.0598	3/8	1
H1	96h	0.2857	0.0207	0.4373	1
H2	96h	0.2974	0.1355	0.3856	1
C1	48g	0.8115	0.6247	0.4388	0.091(1)
H11	96h	0.7607	0.5872	0.4396	0.091(1)
Cl1	96h	0.9013	0.5638	0.4407	0.091(1)

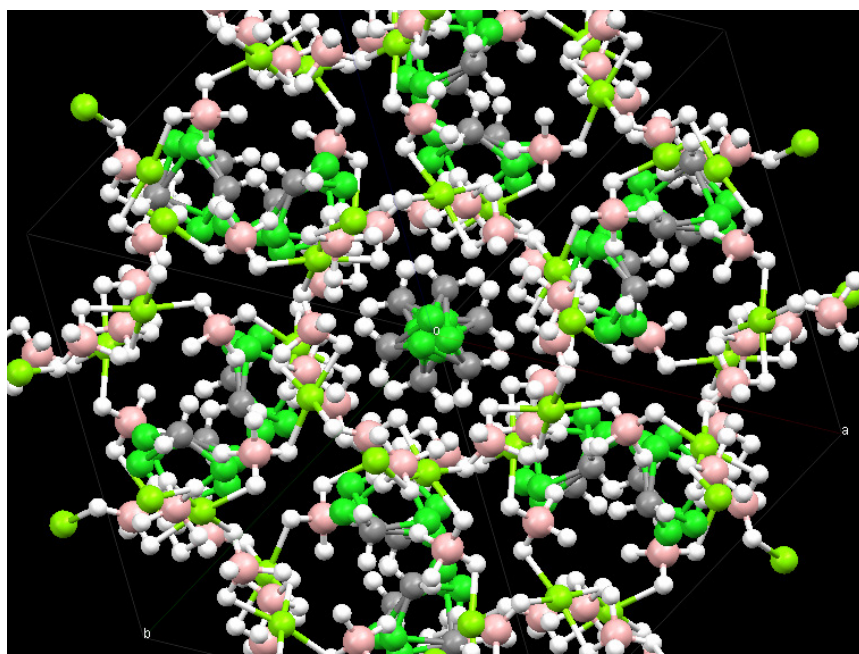


Figure S4. Dichloromethane (CH_2Cl_2) molecules absorbed in the open-pore cubic $\gamma\text{-Mg}(\text{BH}_4)_2$ at ambient temperature are disordered over three equivalent positions around the three-fold symmetry axis. Chlorine atoms are shown as green spheres, carbon atoms as grey, and hydrogen as white spheres. The composition of the host-guest phase, refined from SR-PXD data, is $\text{Mg}(\text{BH}_4)_2 \cdot 0.18 \text{CH}_2\text{Cl}_2$.

7. Absorption-desorption of N_2 and H_2 gases in the porous $\gamma\text{-Mg}(\text{BH}_4)_2$. Nitrogen and hydrogen loading into the porous structure were studied at low temperatures and high pressures. SR-PXD patterns were collected *in-situ* on $\gamma\text{-Mg}(\text{BH}_4)_2$ samples loaded with gasses. A dosing system^{S7} was used to apply gas pressures on the sample up to ca. 100 bar. The samples were enclosed in a 0.5 mm glass capillary under Ar, tightly connected to the dosing system and then outgassed at room temperature to 10^{-3} mbar. One isobar was measured upon desorption (temperature increase) for each of the two gases: at $p(\text{N}_2) = 30.6$ bar, and at $p(\text{H}_2) = 105$ bar, respectively. The temperature was varied from 130 to 325 K for the experiment with nitrogen, and from 80 to 210 K for the experiment with hydrogen using a heating rate of 2 K/min and an Oxford Cryostream 700+. PXD data were collected every 2 min using an X-ray exposure time of 30 s and a readout time of 90 s. Upon the pressure release at ambient temperature the guest molecules are fully desorbed, as monitored by the full recovery of the original intensity ratios in the powder diffraction pattern of $\gamma\text{-Mg}(\text{BH}_4)_2$.

8. Localization of the gas molecules in the porous γ -Mg(BH₄)₂. The position of the nitrogen molecules at 130 K and 30.6 bar was determined using the diffraction data and global optimization in direct space implemented in FOX^{S3}. The structure of the porous Mg(BH₄)₂ framework was fixed, and the position, orientation and occupancy of a nitrogen molecule were optimized. A good fit was achieved with only one crystallographically independent nitrogen molecule, with N-N distance restrained to 1.15(1) Å. No antibump restraints or dynamic occupancy correction were used. The resulting model was refined by Fullprof^{S5}, varying profile and cell parameters, position (orientation fixed) and the occupancy of the nitrogen molecule and the overall atomic displacement. The refined composition of the guest-host structure is Mg(BH₄)₂·0.63N₂. The background was described by linear interpolation between selected points. The final discrepancy factors are: $R_B = 4.2\%$, $R_F = 3.9\%$, $R_p = 9.6\%$, and $R_{wp} = 9.9\%$. The refinement profile is shown in Fig. S5. Crystal data and atomic coordinates are listed in Table S4.

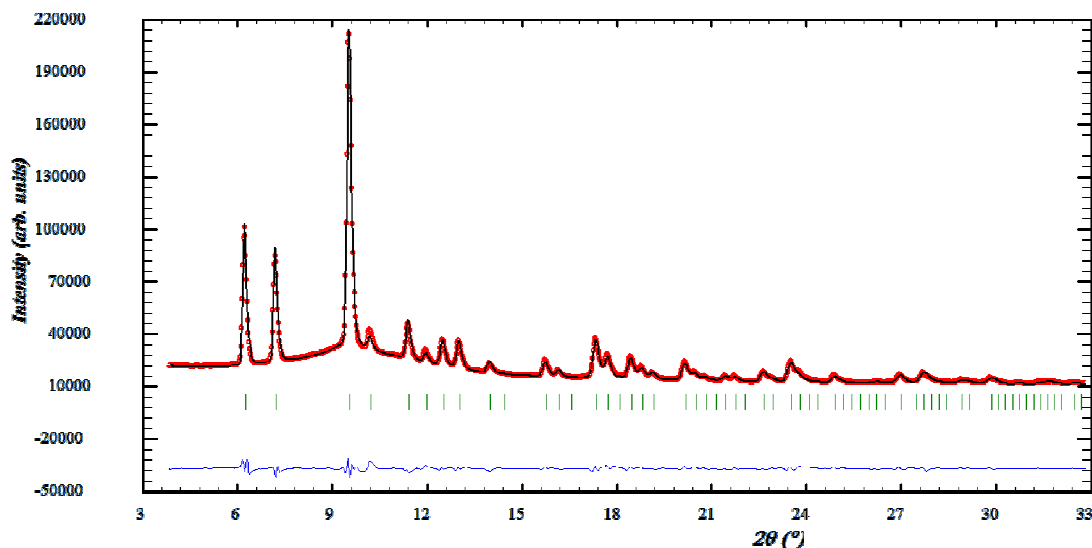


Figure S5. Rietveld refinement profile for γ -Mg(BH₄)₂·0.63N₂ at 130 K under 30.6 bar of N₂. The green marks show Bragg positions ($\lambda = 0.700930$ Å).

Table S4. Experimental structural parameters for γ -Mg(BH₄)₂·0.63N₂ at 130 K under 30.6 bar of N₂. Space group $Ia-3d$, $Z = 24$, $a = 15.7567(7)$ Å, $V = 3912.0(3)$ Å³.

Atom	Wyckoff site	x	y	z	Occupancy
Mg	24d	1/4	1/8	1/2	1
B	48g	0.3098	0.0598	3/8	1

H1	96h	0.2857	0.0207	0.4373	1
H2	96h	0.2974	0.1355	0.3856	1
N1	96h	0.6300(8)	0.6773(12)	0.6674(7)	0.1574(8)
N2	96h	0.6547(8)	0.6360(12)	0.6125(7)	0.1574(8)

The same position of the gas molecule in the porous γ -Mg(BH₄)₂ allowed to satisfactorily model the powder pattern for a hydrogen-loaded sample at 105 bar at 80 K. The hydrogen content, Mg(BH₄)₂·0.80H₂, was estimated from the refinements on the hydrogen-loaded and hydrogen-free samples. The final discrepancy factors for the hydrogen-loaded sample are: $R_B = 7.3\%$, $R_F = 5.0\%$, $R_p = 13.4\%$, and $R_{wp} = 13.5\%$. The refinement profile is shown in Fig. S6.

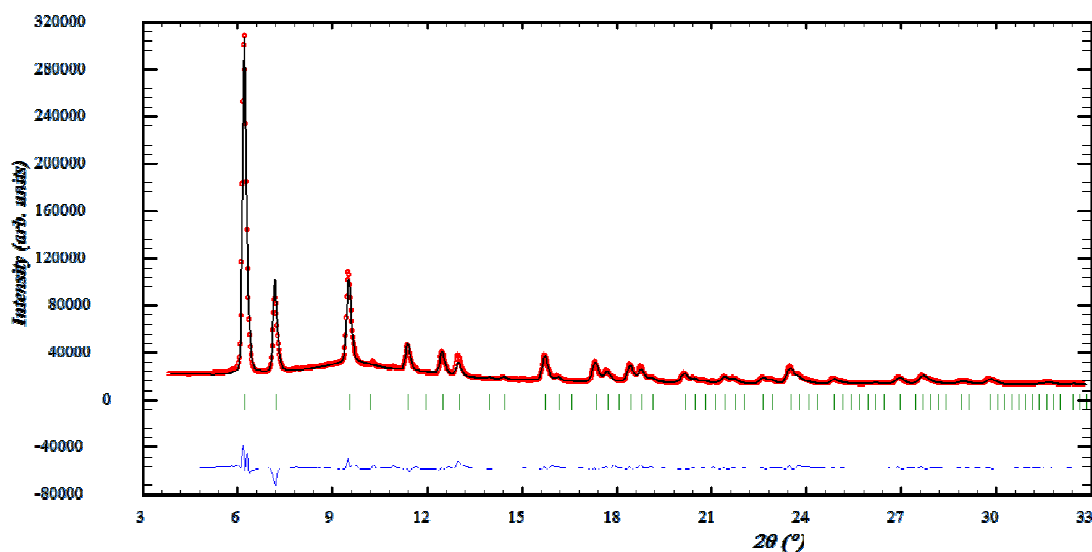


Figure S6. Rietveld refinement profile for γ -Mg(BH₄)₂·0.80H₂ at 80 K under 105 bar of H₂. The green marks show Bragg positions ($\lambda = 0.700930 \text{ \AA}$).

9. Desorption isobars for N₂ and H₂ in the porous γ -Mg(BH₄)₂ determined from *in-situ* synchrotron radiation powder X-ray diffraction data. Rietveld refinement of the occupancies for the structural model described above was based on the *in-situ* powder diffraction data. It yielded desorption isobars shown in Figure 2b in the article. The nitrogen and hydrogen contents on nitrogen- and hydrogen-free samples correspond to zero.

10. High-pressure (HP) diffraction experiments. Transformation of the hexagonal α -Mg(BH₄)₂ and cubic γ -Mg(BH₄)₂ phases under high hydrostatic pressures were studied in diamond anvil cells (DACs) at the Swiss-Norwegian Beam Lines of the ESRF. SR-PXD patterns were collected on the MAR345 image plate detector. A monochromatic beam at a wavelength of $\lambda = 0.770518$ or 0.700400 Å was slit-collimated down to 100×100 μm^2 . Nominal sample-to-detector distances of 200 and 250 mm, beam centre and detector tilts were calibrated using LaB₆ NIST standard. Two-dimensional diffraction images were integrated into 1D patterns using the ESRF Fit2D software^{S1}.

Finely ground samples of the hexagonal or cubic, α - and γ -Mg(BH₄)₂, were loaded into a DAC with flat culets with a diameter of 400-600 μm . In order to prevent a chemical reaction, all manipulations with samples were made in a high-purity argon atmosphere. The samples were loaded into a hole of ~ 200 μm in diameter drilled in stainless steel gaskets pre-indented to ~ 70 μm thickness. Ruby provided a pressure calibration with precision of 0.1 GPa. No pressure-transmitting medium was used for α -Mg(BH₄)₂, while the γ -Mg(BH₄)₂ was compressed both in a dry form and with nitrogen as a pressure-transmitting medium. In both cases, good quasi-hydrostatic conditions were achieved, monitored by a small broadening of the ruby fluorescence peaks. Diffraction measurements for the hexagonal phase were performed up to a maximum pressure of 18.9 GPa, and for the cubic phase up to 4 GPa. In total, five SR-PXD experiments were performed, three on dry α -Mg(BH₄)₂, one on dry γ -Mg(BH₄)₂ and one on γ -Mg(BH₄)₂ in the nitrogen medium. In all compression experiments a new phase, named δ -Mg(BH₄)₂, formed at pressures slightly below 2 GPa.

A decompression experiment on one of the samples showed that the new phase is stable at ambient conditions. Moreover, the pressure-treated sample is not sensitive to air, permitting us to study the temperature evolution of δ -Mg(BH₄)₂ at ambient pressure. For that, a gasket with the sample was removed from the DAC and heated by a hot air blower, while the transformations in the sample were monitored by *in-situ* SR-PXD. The temperature was measured by a thermocouple mounted on the metallic gasket.

11. Structure solution and refinement for the HP tetragonal δ -Mg(BH₄)₂. A SR-PXD pattern of the high-pressure phase was indexed in a primitive tetragonal phase using DICVOL2004^{S2}. The structure has been solved in the space group $P4_2$, using FOX^{S3} optimizing a position of one Mg atom and the position and orientation of a rigid tetrahedral borohydride group. Antibump restraints of 1.8 Å were used for Mg-H distances. The true $P4_2nm$ symmetry was determined using ADDSYM procedure in Platon^{S4} and the model was refined by Rietveld method using Fullprof Suite^{S5}. Coordinates of the magnesium atom were

fixed in (0, 0, 0) position, while B and H atoms were refined using restraints on the B-H distances (1.22 Å) and H-B-H angles (109.5°). A preferred orientation along [001] and an orthorhombic strain in the tetragonal lattice were modelled by one refined parameter each. The background was described by linear interpolation between selected points. For the diffraction data collected on δ -Mg(BH₄)₂ at ambient pressure and 295 K, the final discrepancy factors are: $R_B = 9.7\%$, $R_F = 7.5\%$, $R_p = 17.1\%$, and $R_{wp} = 13.9\%$. The refinement profile is shown in Fig. S7. Crystal data and atomic coordinates are listed in Table S5.

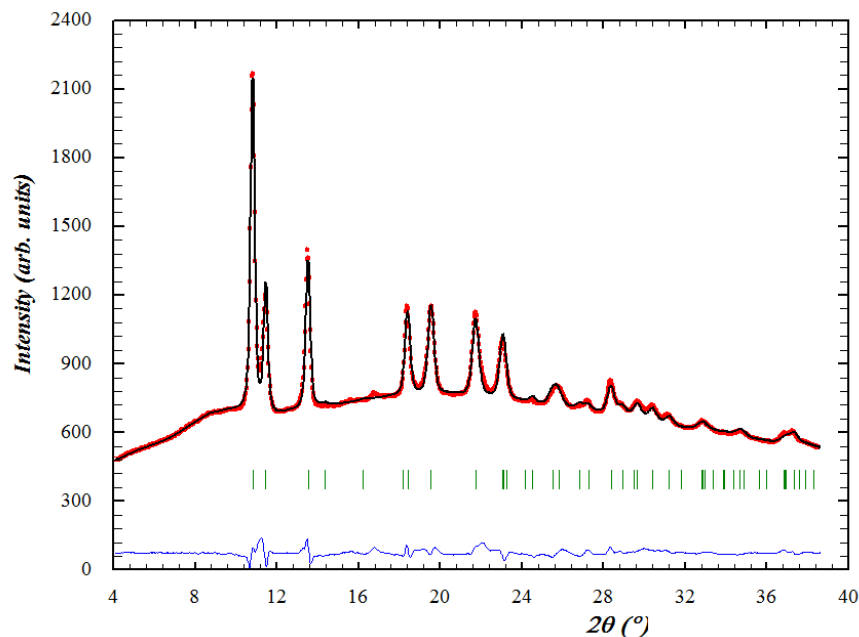


Figure S7. Rietveld refinement profile for δ -Mg(BH₄)₂ quenched to the ambient pressure. The green marks show Bragg positions ($\lambda = 0.770518$ Å).

Table S5. Experimental structural parameters for the tetragonal δ -Mg(BH₄)₂ at ambient conditions. Space group $P4_2nm$, $Z = 2$, $a = 5.4361(10)$, $c = 6.1468(12)$ Å, $V = 181.63(6)$ Å³.

Atom	Wyckoff site	x	y	z
Mg	$2a$	0	0	0
B	$4c$	0.2584(4)	x	0.2432(4)
H1	$8d$	0.2050(9)	0.4641(5)	0.3048(8)
H2	$4c$	0.1122(4)	x	0.3185(11)
H3	$4c$	0.2525(9)	x	0.0460(4)

12. Pressure-induced phase transitions in α -, γ - and δ -Mg(BH₄)₂. Upon compression of the α -Mg(BH₄)₂ to 1.1-1.6 GPa, a phase transition to the δ -Mg(BH₄)₂ is observed, in agreement with the previous experimental data^{S8}. A second phase transformation from δ -Mg(BH₄)₂ to a new phase, denoted ϵ -Mg(BH₄)₂, with a yet unknown structure, occurs at 17 GPa. ϵ -Mg(BH₄)₂ is presumably a slightly more dense polymorph as compared to δ -Mg(BH₄)₂. The latter phase transition is reversible, and the δ -Mg(BH₄)₂ is fully recovered on decompression to 14 GPa. The high-pressure phase, δ -Mg(BH₄)₂, is stable upon the decompression to the ambient conditions.

Compression of the dry open-pore γ -Mg(BH₄)₂ first leads to an amorphisation, illustrated in the diffraction pattern by the disappearance of the Bragg peaks and by an emerging modulated background characteristic for the amorphous state (Figure 3b in the article). The amorphisation starts at 0.4 GPa, when the intensities of the Bragg peaks decrease in intensity and the amorphous halo appears at the d -spacing of 4.78 Å. At 0.9 GPa, the Bragg peaks of γ -Mg(BH₄)₂ fully disappear, and the halo moves to lower d -spacing of 4.55 Å. At 2.1 GPa, the crystalline δ -phase appears and the position of the remaining amorphous halo moves to 4.30 Å. Compression of γ -Mg(BH₄)₂ in nitrogen as pressure-transmitting medium shows essentially the same behaviour, i.e. complete amorphization at ~1 GPa and the appearance of the crystalline δ -Mg(BH₄)₂ at 2.2 GPa.

Diffraction-amorphous Mg(BH₄)₂ has recently been synthesized by high-energy ball-milling of MgB₂ in H₂ atmosphere^{S9}, showing the same characteristic broad peak with d -spacing of 4.89 Å at ambient conditions. It remains to be established if the two diffraction-amorphous phases are identical.

13. Equations of state and volume collapses for α -, γ - and δ -Mg(BH₄)₂. The unit cell volumes for the three phases in the five compression experiments were fitted by the Murnaghan equation of state:

$$V(P) = V_0 \left(1 + B'_0 \frac{P}{B_0} \right)^{-1/B'_0},$$

where B_0 is a bulk modulus, B'_0 is the first pressure derivative of bulk modulus (fixed at 5.8 for all phases), and V_0 is a molar volume at zero pressure. Variation of the volume of the Mg(BH₄)₂ formula unit in α - and δ -phases at ambient temperature and the compressibility data are shown in Figure S8. Variation of the volume of the Mg(BH₄)₂ formula unit in γ - and δ -phases at ambient temperature and the compressibility data is shown in Figure S9. The compressibility data for the γ -phases were determined only on five points measured at pressures up to 0.5 GPa.

We note that the bulk modulus of the δ -phase (28.5 GPa) is almost three times higher than that (10.2 GPa) reported by George *et al.*^{S8} The volume drop stated in Ref. S8 is not comparable to our data, since the unit cell for the high-pressure phase was incorrectly determined. We determined for the first time the bulk modulus for the α - and γ -phases to 10.9 and 12.7 GPa, respectively, which are the lowest values among all the studied metal borohydrides^{S10}. In particular, they are lower than for the ambient-pressure phase of LiBH_4 (14.4 GPa)^{S11} and comparable to the bulk modulus of ammonia-borane, NH_3BH_3 (9.9 GPa)^{S12}.

δ - $\text{Mg}(\text{BH}_4)_2$ is stable upon decompression and has 20.7 % and 44 % smaller volume than that of α - and γ - $\text{Mg}(\text{BH}_4)_2$, respectively, measured at ambient conditions. These are the largest pressure-induced volume collapses found in hydrides, and are among the largest known for inorganic materials, for instance comparable to 35 % volume change from graphite to diamond.

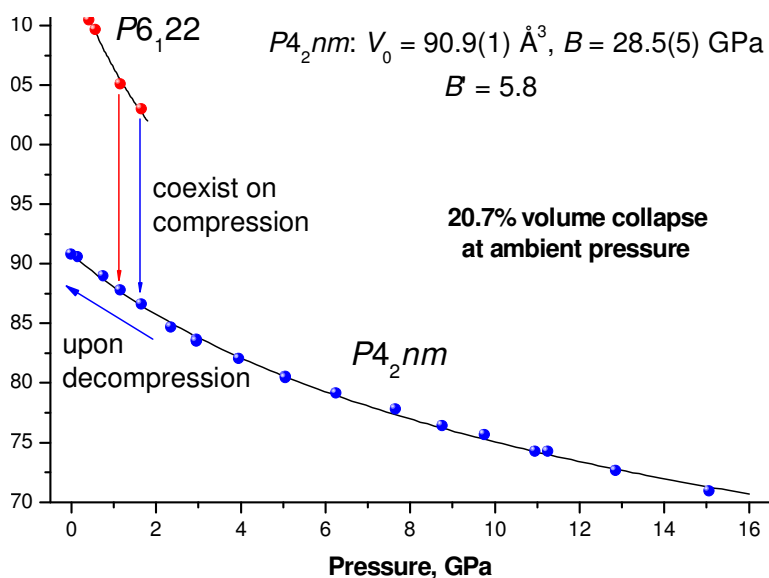


Figure S8. The volume per formula unit of $\text{Mg}(\text{BH}_4)_2$ measured upon compression of α - $\text{Mg}(\text{BH}_4)_2$ at ambient temperature. The circles represent experimental data, and the lines are the best fits to the Murnaghan equation of state. δ - $\text{Mg}(\text{BH}_4)_2$ is stable upon decompression and has 20.7 % smaller volume than that of the α -phase measured at ambient conditions.

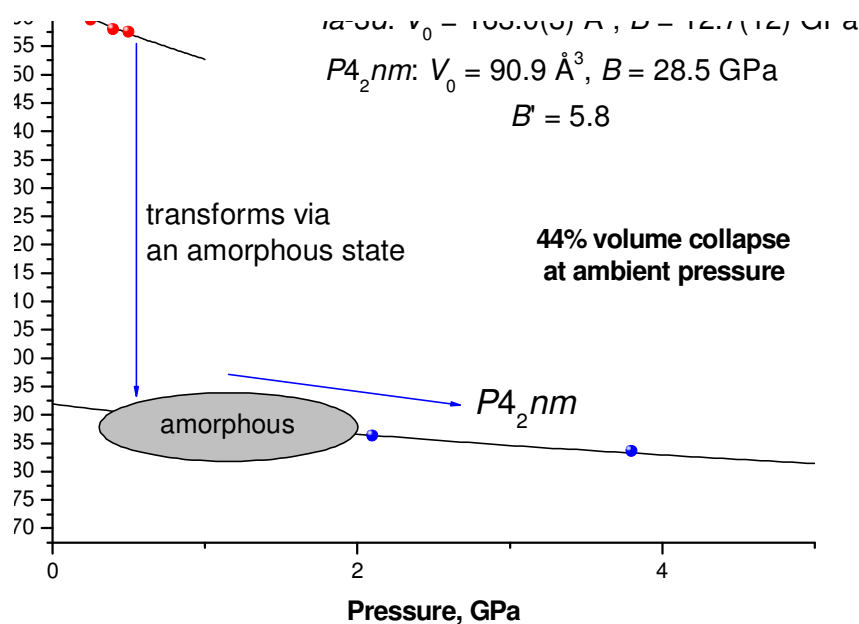


Figure S9. Variation of the unit cell volume per formula unit of $\text{Mg}(\text{BH}_4)_2$ upon compression of the porous $\gamma\text{-Mg}(\text{BH}_4)_2$ at ambient temperature. The circles represent experimental data, and the lines are the best fits to the Murnaghan equation of state. At ambient conditions, $\delta\text{-Mg}(\text{BH}_4)_2$ has 44 % smaller volume than that of $\gamma\text{-Mg}(\text{BH}_4)_2$.

14. Pressure and temperature evolution of $\delta\text{-Mg}(\text{BH}_4)_2$.

The high-pressure $\delta\text{-Mg}(\text{BH}_4)_2$ phase is a tetragonally distorted antitype of the cubic Cu_2O structure (space group $Pn\bar{3}m$). The group subgroup relations are as following: $P4_2nm$ (No. 102) is a subgroup of index 2 of $P4_2/nmm$ (No. 134, inversion center added on the B atom), the latter is a subgroup of index 3 of $Pn\bar{3}m$ (No. 224). The c/a ratio is a measure of the tetragonal distortion of the cubic structure, and we studied its evolution with pressure and temperature. Figure S10 shows that the a and c parameters vary nonlinearly with pressure, while the c/a ratio increases proportionally to the square root of pressure (from 1.13 at ambient pressure to 1.255 at 16.2 GPa), indicating that the deformation is the order parameter of the tetragonal distortion.

Upon heating at ambient pressure, the c/a ratio for $\delta\text{-Mg}(\text{BH}_4)_2$ decreases (Figure S11). Moreover, the thermal expansion in the basal plane is positive, while along the c -axis it is negative (Figure S11). It is remarkable that the diffraction patterns of $\delta\text{-Mg}(\text{BH}_4)_2$ show some residual intensity between the tetragonally-split Bragg peaks of the parent cubic phase (tetragonal $hkl = 101$ and 110 ; 202 and 220). This indicates a likely presence of a non-distorted cubic phase similar to $\delta\text{-Mg}(\text{BH}_4)_2$, which can be identified

as yet another new $\text{Mg}(\text{BH}_4)_2$ polymorph, here denoted δ' - $\text{Mg}(\text{BH}_4)_2$. At about 100°C the δ -phase transforms into the α -phase, which remains stable on cooling.

We note that the high-pressure δ -phase may likely be obtained by high-energy ball milling of other $\text{Mg}(\text{BH}_4)_2$ polymorphs. For instance, the β - $\text{Mg}(\text{BH}_4)_2$ ball-milled with 10% of silica or alumina, yields a product^{S13} with a powder diffraction pattern similar to the one of the δ - $\text{Mg}(\text{BH}_4)_2$. This product slowly transforms into the α -phase.

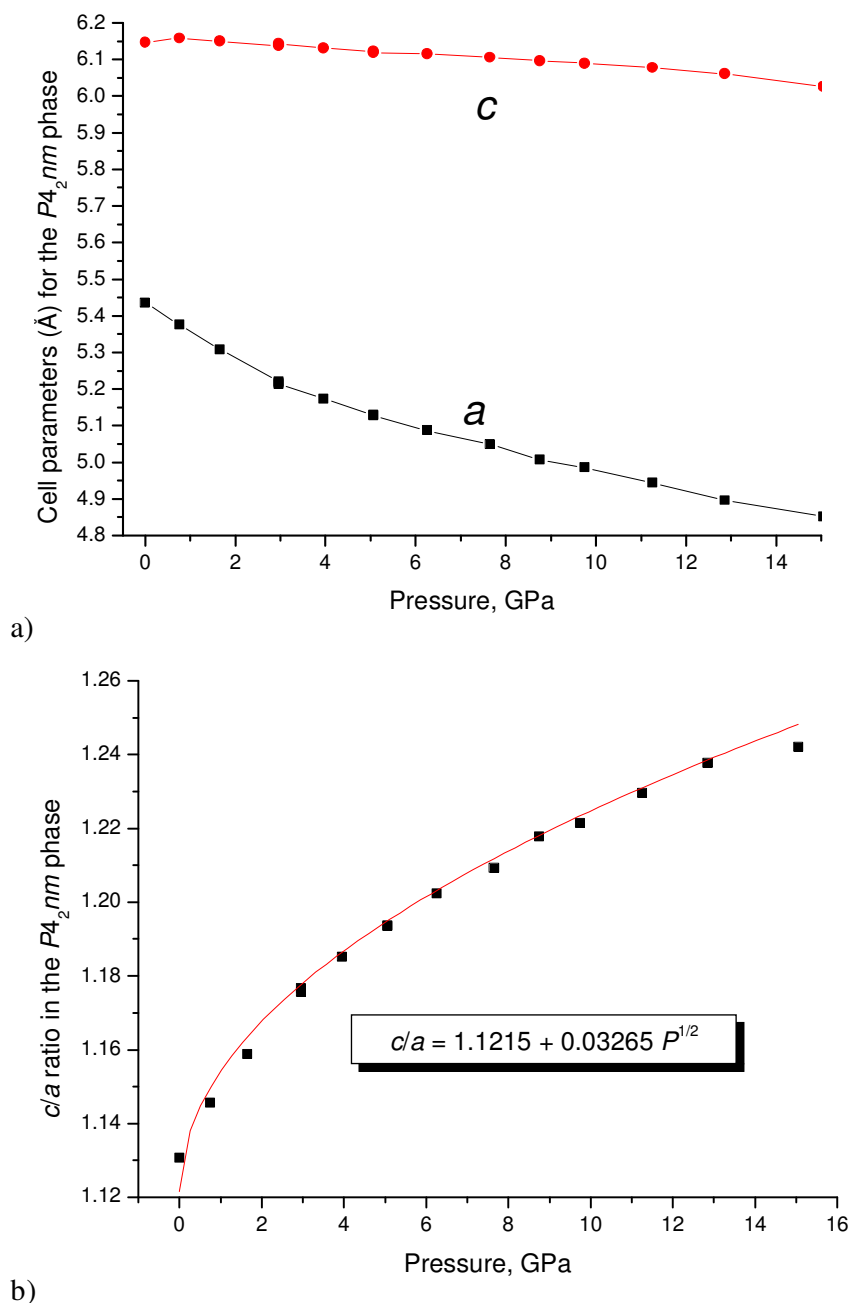
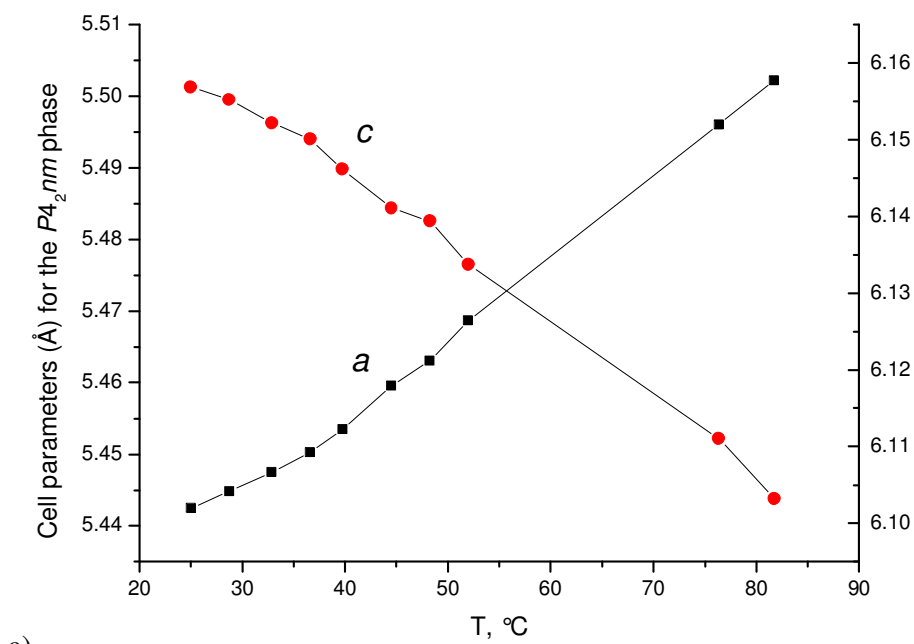
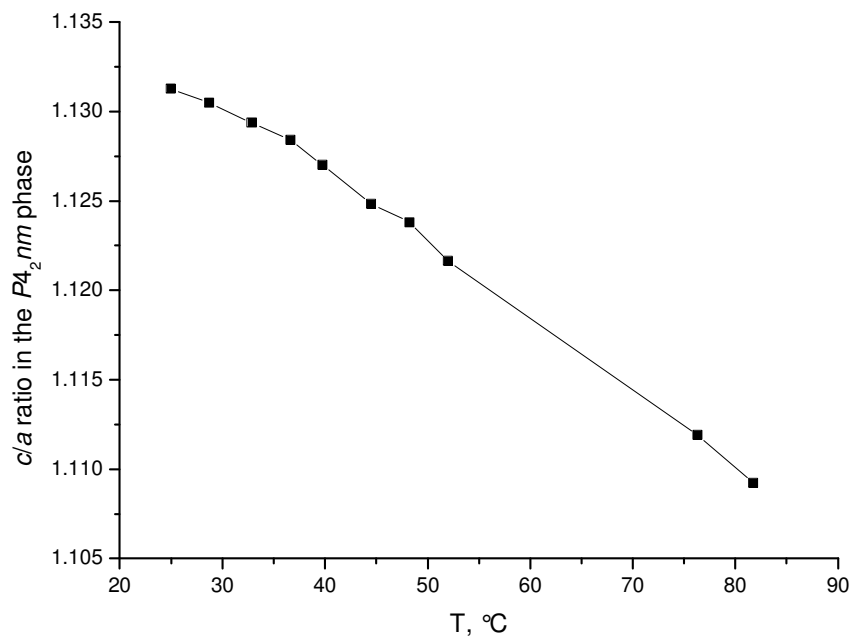


Figure S10. Pressure dependence of the cell parameters (a) and of the c/a ratio (b) for δ - $\text{Mg}(\text{BH}_4)_2$ at ambient temperature. The tetragonal distortion of the cubic Cu_2O -antitype structure is more pronounced at higher pressures, following the simple square root equation.



a)



b)

Figure S11. Temperature dependence of the cell parameters (a) and of the c/a ratio (b) for $\delta\text{-Mg}(\text{BH}_4)_2$ quenched to the ambient pressure. The tetragonal distortion of the cubic Cu_2O -antitype structure is more pronounced at lower temperatures.

15. Geometry of MgH₈ polyhedra in the experimental and the most stable theoretically predicted Mg(BH₄)₂ structures.

Table S6. Characteristics of the coordination polyhedra in the experimental and in the most stable theoretically predicted Mg(BH₄)₂ structures. The number of a Johnson solid^{S14} is indicated where appropriate.

Phase / symmetry	Geometry of MgH ₈ , Johnson solid	Point gr.	References
Experimental structures			
α / <i>P6₁22</i>	Snub disphenoid, J ₈₄ (three Mg)	D _{2d}	S15
β / <i>Fddd</i>	Biaugmented triangular prism, J ₅₀ (one Mg)	D _{2v}	S16, S17
	Gyrobifastigium, J ₂₆ (one Mg)	D _{2d}	
γ / <i>Ia-3d</i>	Snub disphenoid, J ₈₄ (one Mg)	D _{2d}	This work
δ / <i>P4₂nm</i>	Elongated triangular dipyramid, J ₁₄ (one Mg)	D _{3h}	This work
Theoretically predicted structures			
<i>I-4m2</i>	Cube (one Mg)	O _h	S18-S20
<i>I4₁22</i>	Cube (one Mg)	O _h	S19
<i>F222</i>	Snub disphenoid, J ₈₄ (one Mg)	D _{2d}	S21, S19
	Cube (one Mg)	O _h	
<i>I4₁/amd</i>	Snub disphenoid, J ₈₄ (one Mg)	D _{2d}	S21
	Cube (one Mg)	O _h	

16. Characterization of γ -Mg(BH₄)₂ surface area and pore size by physisorption of nitrogen.

Characterization of surface area, pore volume and size in γ -Mg(BH₄)₂ was made using Micromeritics ASAP 2020 Surface Area and Porosity Analyzer. The sample was transferred under argon and outgassed under vacuum at 310 K prior to the measurement. The characterization was carried out at 78.2 K using nitrogen gas.

The first experiment, aiming to determine the absorption capacity and the cumulative surface area, was conducted on 79.1 mg sample, in the pressure range from 0 to 11 mbar. The absorption capacity reached a plateau of 154 cm³/g STP already at ~1 mbar. Achieving equilibrium at so low pressures required long time, thus the whole experiments took 5 days and then was stopped due to the use up of liquid nitrogen.

The second experiment, aiming for BET surface characterization and for determination of the absorption pore area, was carried out on a smaller sample (27.1 mg), in the range from 0 to 1 bar, and was completed in 2 days.

Absorption capacity (Fig. S12) at 1 mbar and 78 K corresponds to the composition $\gamma\text{-Mg}(\text{BH}_4)_2 \cdot 0.37\text{N}_2$, which is in a fairly good agreement with the slightly higher capacity ($\gamma\text{-Mg}(\text{BH}_4)_2 \cdot 0.63\text{N}_2$) at much higher pressure of 30.6 bar, obtained from the diffraction data at 80 K. The cumulative surface area was estimated by MP-method at $1160 \text{ m}^2/\text{g}$, using $1.96\text{-}2.6 \text{ \AA}$ pore hydraulic radius interval.

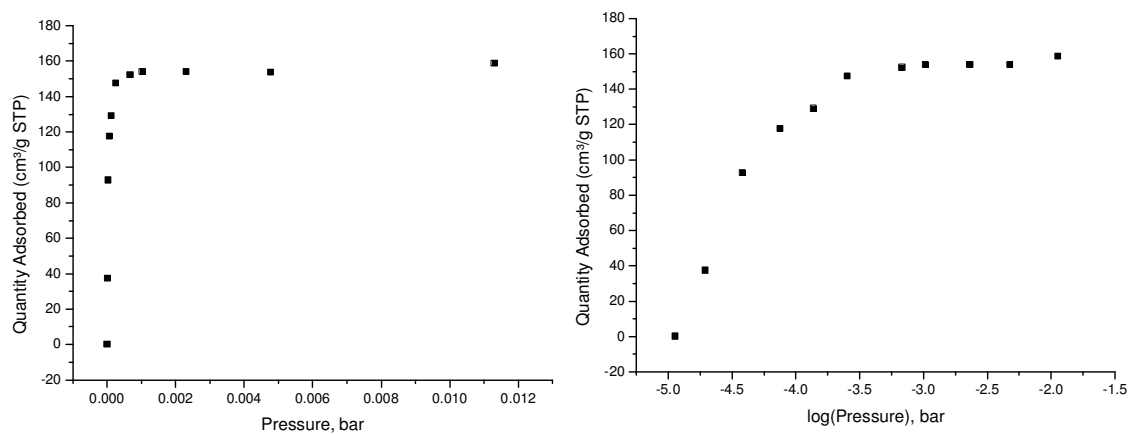


Figure S12. Quantity of adsorbed nitrogen as a function of pressure at 78 K in linear (a) and in log(P) (b) scales.

Despite the BET surface area plot shows nearly perfect linearity (correlation coefficient is 0.9992, see Fig. S13), the obtained value of the surface area ($246(4) \text{ m}^2/\text{g}$) likely does not represent the true surface area for this very small pore system: only very little quantity of nitrogen is adsorbed at pressures above 0.06 bar, i.e. $1.3 \text{ cm}^3/\text{g N}_2 \text{ STP}$ on pressure increase from 0.07 to 0.2 bar. Barret-Joyner-Halenda (BJH) adsorption dV/dD pore volume (Fig. S14) and dA/dD pore area plots show a maximum at pore size of 7.5 \AA . This number is in good agreement with the size of pores outlined by the structural determination from diffraction data (Fig. 1b).

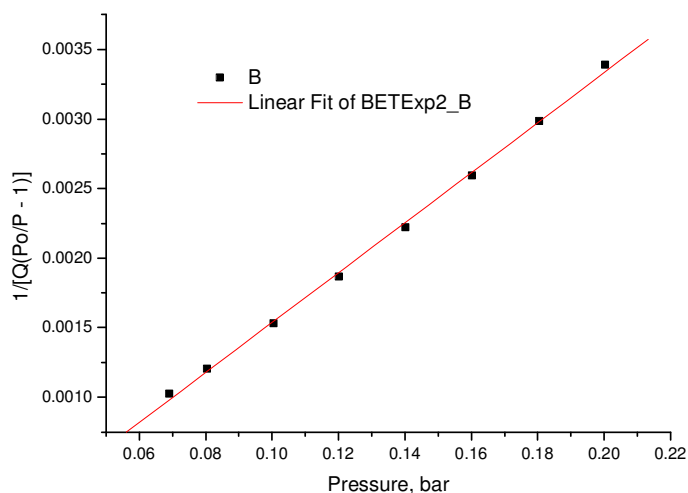


Figure S13. BET surface area plot revealing a value of x m²/g for the sample of γ -Mg(BH₄)₂.

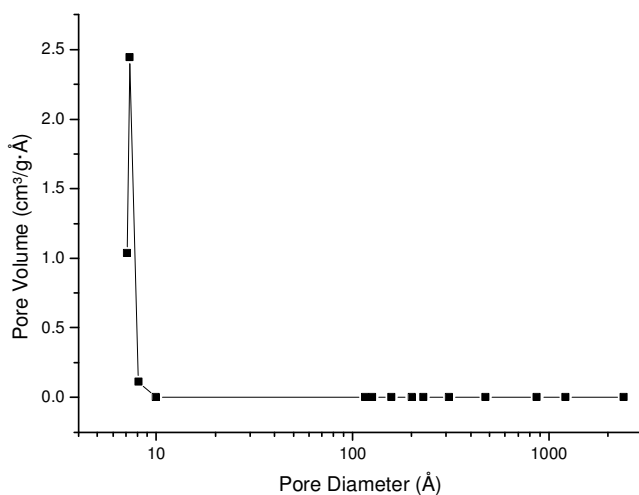


Figure S14. BJH Adsorption dV/dD pore volume distribution, indicating the presence of only one type of pores of a very small size, ~ 7 Å.

17. Calculation of surface area and pore volume and size in γ -Mg(BH₄)₂ from the crystal structure.

An unoccupied void of ~ 79 Å³ was detected by PLATON using 2.0 Å probe. 16 symmetry-related voids per unit cell make $\sim 33\%$ of the free volume (corresponding to the pore volume of 0.60 mL/g). The voids have an ellipsoidal shape with axial ratios 1.31:1:1. When accessibility to water is being assessed, it is usual to use 1.4 Å as the standard radius of the solvent molecule (it also serves as the default value for AREAIMOL and SURFACE programs). The principle axes of the ellipsoid defined by the centre of the 1.4 Å probe are 1.79 Å x 1.03 Å x 1.03 Å and the accessible surface area is 20.23 Å² per void. This corresponds to 1505 m²/g of the accessible surface. The effective radius of the nitrogen molecule is

somewhat larger, so the respective accessible surface area for N₂ is expected to be smaller. Thus, 1505 m²/g solvent-accessible area compares well with 1160 m²/g cumulative surface area obtained by the MP-method.

18. Determination of isosteric heats of N₂ and H₂ adsorption in γ -Mg(BH₄)₂, using *in-situ* diffraction data collected through a set of isobars.

In-situ powder diffraction data collected under nitrogen and hydrogen atmosphere were used to determine the amount of N₂ and H₂ molecules in γ -Mg(BH₄)₂. Three isobars were measured for nitrogen and two for hydrogen, with pressure range spanning 1.5-2 orders of magnitude. Oxford Cryostream 700+ was used to automatically control the temperature. All the isotherms were measured upon heating at 120 K/h rate. Refined occupancies were converted to the number of X₂ molecules per Mg atoms and plotted in Figs. S15 and S16.

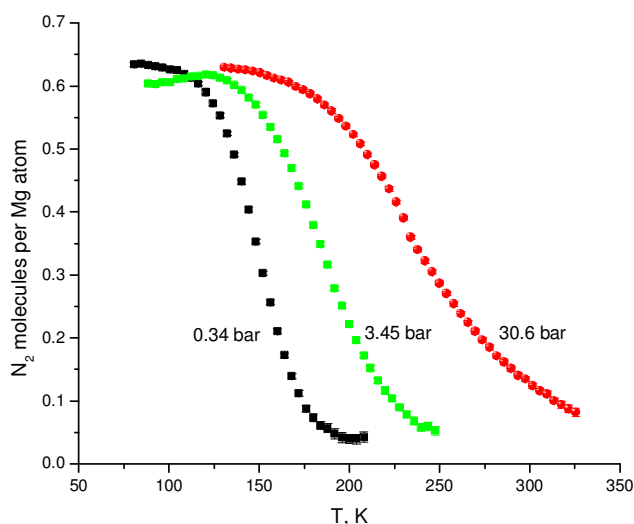


Figure S15. Amount of adsorbed nitrogen in γ -Mg(BH₄)₂ extracted from *in-situ* powder diffraction data measured through a set of three isobars.

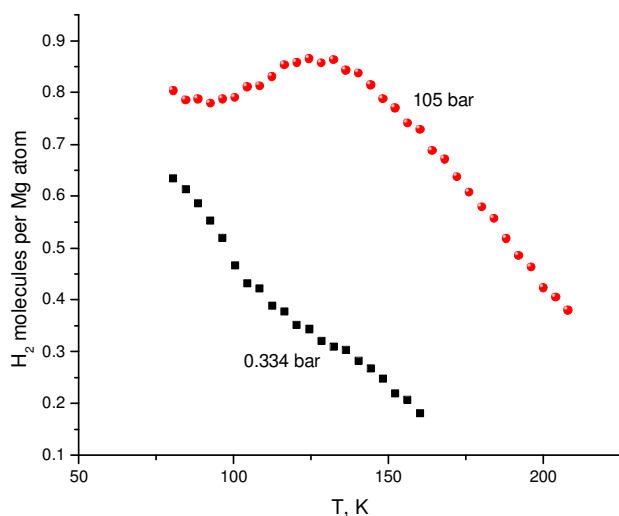


Figure S16. Amount of adsorbed hydrogen in γ -Mg(BH₄)₂ extracted from *in-situ* powder diffraction data measured through a set of two isobars.

The following expression derived from the Clausius–Clapeyron equation was used to estimate the absorption enthalpy from the isobars: $\ln \frac{P_1}{P_2} = \frac{\Delta h}{R} \left(\frac{1}{T_2} - \frac{1}{T_1} \right)$.

In order to be able to use this expression, the P₁-T₁ and P₂-T₂ conditions from two different isobars must correspond to exactly the same amount of the adsorbed gas. Therefore we interpolated the composition - temperature to a fixed grid of compositions at all pressures. For that, the dependence of the adsorbed

quantity of gas versus temperature was fitted by the Logistic function of growth, $y = \frac{A_1 - A_2}{1 + (x/x_0)^p} + A_2$.

Then the analytical expression was used to calculate temperatures for the grid of compositions. At each composition, an isosteric (at the fixed composition) heat of adsorption was calculated. The dependence of the isosteric heat versus the composition is plotted in Fig. S17. We show only a part of the compositional range where the fit of the analytical expression to the data is good. For nitrogen, the isosteric heat of nitrogen adsorption Q_{st} (N₂) is nearly constant with loading, with the average value of = 14.7(3) kJ/mol. For hydrogen Q_{st} (H₂) varies from 7.5 to 4.5 kJ/mol, with an average estimate of 6 kJ/mol. Other models of interpolation will be tested and more accurate values of Q_{st} will be presented in our future work.

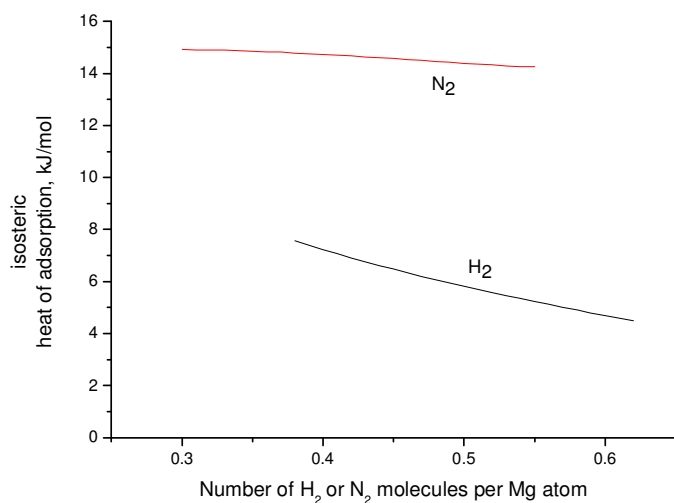


Figure S17. A plot of the isosteric heat of adsorption of nitrogen and hydrogen in γ -Mg(BH₄)₂ as a function of composition (gas loading).

19. Comparison of IR and Raman spectra for the amorphous and crystalline Mg(BH₄)₂.

We assume that similar to zeolitic imidazolate frameworks [S22], there is no polyamorphism in Mg(BH₄)₂. Therefore, we performed a detailed spectroscopic characterization of the amorphous Mg(BH₄)₂ prepared by ball-milling. The amorphous Mg(BH₄)₂ samples were prepared by ball milling γ -Mg(BH₄)₂ for 2 hours (sample "M") and 4 hours (sample "B"). Diffraction experiments showed that the "M" sample contained some residual diffraction peaks of the crystalline phase, while the "B" sample shows only broad amorphous humps with an intensity maximum at ~ 4.7 Å, similar to the pressure-collapsed amorphous phase (see Fig. 3b in the main text).

IR spectra (Fig. S18) were recorded at room temperature using a Biorad Excalibur instrument equipped with a Specac Golden Gate ATR cell. The nominal resolution was set to 1 cm⁻¹. Raman spectra (Fig. S19) were measured at room temperature using a 488 nm laser, and a Kaiser Optical Holospec monochromator in conjunction with a liquid nitrogen cooled CCD camera.

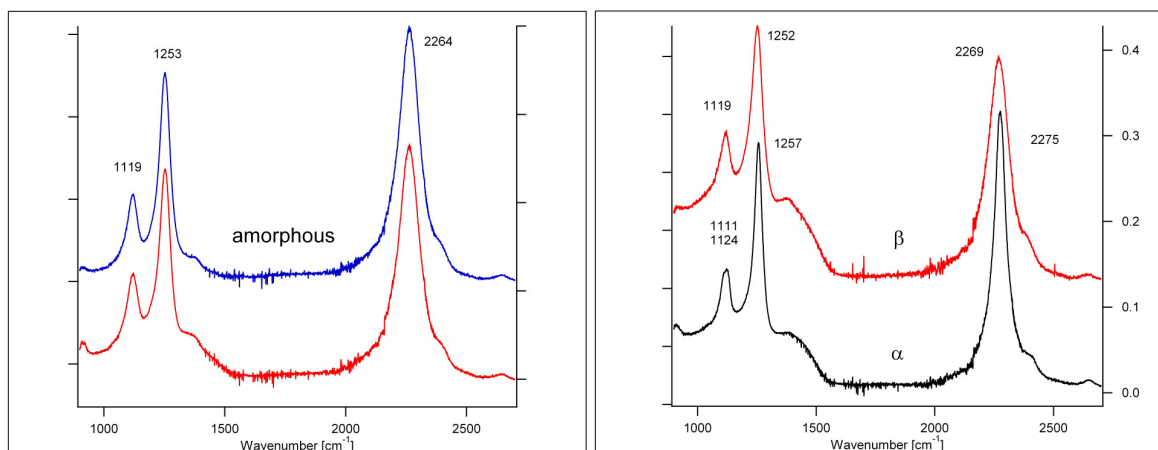


Figure S18. IR spectra of the amorphous $\text{Mg}(\text{BH}_4)_2$ (left square) - "M" (red) and "B" (blue); and of the crystalline $\text{Mg}(\text{BH}_4)_2$ (right square) - α -phase (black) and β -phase (red).

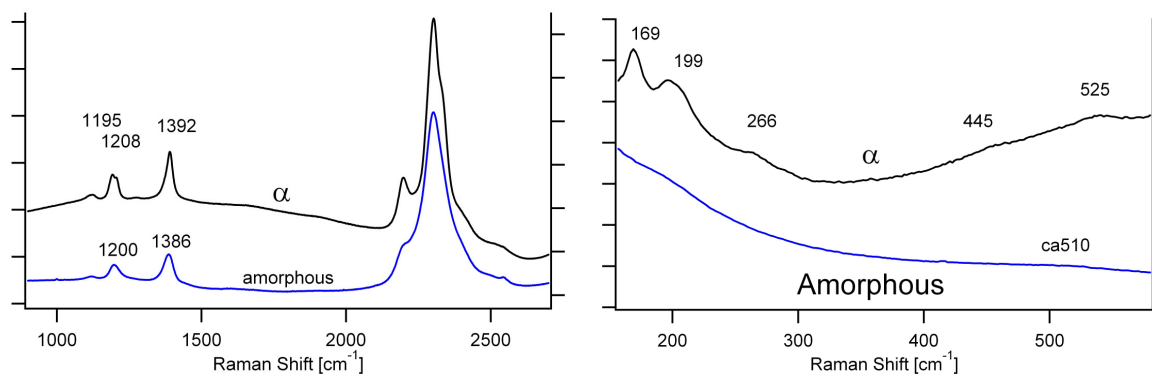


Figure S19. Raman spectra of the amorphous ("B") and crystalline (α -phase) $\text{Mg}(\text{BH}_4)_2$ in the region of internal modes (left) and in the region of lattice modes (right).

The comparison of the IR spectra shows that there are only very small differences between the amorphous and two crystalline $\text{Mg}(\text{BH}_4)_2$ phases, i.e. the local structure of the amorphous material remains the same as in the crystalline forms. This observation is also true for the Raman spectra, which show almost no difference for the internal modes. Instead, the lattice mode region for the amorphous phase contains no features, while the crystalline phase shows well pronounced lattice modes (around 200 cm^{-1}) as well as very weak librational modes. Careful inspection of the spectrum suggests a possible presence of a very weak band around 510 cm^{-1} for the amorphous sample. This spectral region corresponds to librational motions of the BH_4 -group. This observation confirms that the amorphous phase is lacking long range order but keeps the features of the crystalline state at the local level.

20. References

- S1. Hammersley, A. P., Svensson, S. O., Hanfland, M., Fitch, A. N. & Häusermann, D. Two-dimensional detector software: From real detector to idealised image or two-theta scan. *High Pressure Res.* **14**, 235-248 (1996).
- S2. Boultif, A. & Louer, D. Powder pattern indexing with the dichotomy method. *J. Appl. Cryst.* **37**, 724-731 (2004).
- S3. Favre-Nicolin, V. & Cerný, R. FOX, 'free objects for crystallography': a modular approach to ab initio structure determination from powder diffraction. *J. Appl. Cryst.* **35**, 734-743 (2002).
- S4. Spek, A.L. PLATON, An Integrated Tool for the Analysis of the Results of a Single Crystal Structure Determination *Acta Cryst. A* **46** (Supplement), C34 (1990).
- S5. Rodríguez-Carvajal, J. Recent advances in magnetic structure determination by neutron powder diffraction. *Physica B* **192**, 55-69 (1993).
- S6. Altomare, A., Camalli, M., Cuocci, C., Giacovazzo, C., Moliterni, A. & Rizzi, R. EXPO2009: structure solution by powder data in direct and reciprocal space. *J. Appl. Cryst.* **42**, 1197-1202 (2009).
- S7. a) Llewellyn, P. L., Horcajada, P., Maurin, G., Devic, T., Rosenbach, N., Bourrelly, S., Serre, C., Vincent, D., Loera-Serna, S., Filinchuk, Y. & Férey, G. Complex Adsorption of Short Linear Alkanes in the Flexible Metal-Organic-Framework MIL-53(Fe). *J. Am. Chem. Soc.* **131**, 13002-13008 (2009); b) Jensen, T. R., Nielsen, T. K., Filinchuk, Y., Jørgensen, J.-E., Cerenius, Y., MacA. Gray, E. & Webb, C. J. Versatile in situ powder X-ray diffraction cells for solid-gas investigations. *J. Appl. Cryst.* **43**, 1456-1463 (2010).
- S8. George, L., Drozd, V., Saxena, S. K., Bardaji, E. G. & Fichtner, M. Structural Phase Transitions of $\text{Mg}(\text{BH}_4)_2$ under Pressure. *J. Phys. Chem. C* **113**, 486-492 (2009).
- S9. Pistidda, C., Garroni, S., Dolci, F., Bardaji, E. G., Khandelwal, A., Nolis, P., Dornheim, M., Gosalawit, R., Jensen, T., Cerenius, Y., Surinach, S., Baro, M. D., Lohstroh, W. & Fichtner, M. Synthesis of amorphous $\text{Mg}(\text{BH}_4)_2$ from MgB_2 and H_2 at room temperature. *J. Alloys. Comp.* **508**, 212-215 (2010).
- S10. Filinchuk, Y., Chernyshov, D. & Dmitriev, V. Light metal borohydrides: crystal structures and beyond. *Z. Kristallogr.* **223**, 649-659 (2008).
- S11. Filinchuk, Y., Chernyshov, D., Nevidomskyy, A. & Dmitriev, V. High-pressure polymorphism as a step towards destabilization of LiBH_4 . *Angew. Chem. Int. Ed.* **47**, 529-532 (2008).
- S12. Filinchuk, Y., Nevidomskyy, A., Chernyshov, D. & Dmitriev, V. High-pressure phase and transition phenomena in ammonia borane NH_3BH_3 from x-ray diffraction, Landau theory, and ab initio calculations. *Phys. Rev. B* **79**, 214111 (11pages) (2009).

- S13. Soloveichik, G. L., Andrus, M., Gao, Y., Zhao, J.-C. & Kniajanski, S. Magnesium borohydride as a hydrogen storage material: Synthesis of unsolvated $\text{Mg}(\text{BH}_4)_2$. *Int. J. Hydrogen Energy* **34**, 2144-2152 (2009).
- S14. Johnson, N. W. Convex polyhedra with regular faces. *Can. J. Math.* **18**, 169-200 (1966).
- S15. Filinchuk, Y., Černý, R. & Hagemann, H. Insight into $\text{Mg}(\text{BH}_4)_2$ with Synchrotron X-ray Diffraction: Structure Revision, Crystal Chemistry, and Anomalous Thermal Expansion. *Chem. Mater.* **21**, 925-933 (2009).
- S16. Her, J.-H., Stephens, P. W., Gao, Y., Soloveichik, G. L., Rijssenbeek, J., Andrus, M. & Zhao, J.-C. Structure of unsolvated magnesium borohydride $\text{Mg}(\text{BH}_4)_2$, *Acta Cryst. B* **63**, 561-568 (2007).
- S17. Dai, B., Sholl, D. S. & Johnson, J. K. First-Principles Study of Experimental and Hypothetical $\text{Mg}(\text{BH}_4)_2$ Crystal Structures. *J. Phys. Chem. C* **112**, 4391-4395 (2008).
- S18. Ozolins, V., Majzoub, E. H. & Wolverton, C. First-Principles Prediction of a Ground State Crystal Structure of Magnesium Borohydride. *Phys. Rev. Lett.* **100**, 135501 (4 pages) (2008).
- S19. Zhou, X.-F., Qian, Q.-R., Zhou, J., Xu, B., Tian, Y. & Wang, H.-T. Crystal structure and stability of magnesium borohydride from first principles. *Phys. Rev. B* **79**, 212102 (4 pages) (2009).
- S20. Caputo, R., Tekin, A., Sikora, W. & Züttel, A. First-principles determination of the ground-state structure of $\text{Mg}(\text{BH}_4)_2$. *Chem. Phys. Lett.* **480**, 203-209 (2009).
- S21. Voss, J., Hummelshøj, J. S., Łodziana, Z. & Vegge, T. Structural stability and decomposition of $\text{Mg}(\text{BH}_4)_2$ isomorphs – an ab initio free energy study. *J. Phys.: Condens. Matter* **21**, 012203 (7 pages) (2009).
- S22. Bennett, T. D., Keen, D. A., Tan, J.-C., Barney, E. R., Goodwin, A. L., Cheetham, A. K. Thermal amorphization of zeolitic imidazolate frameworks. *Angew. Chem., Int. Ed.*, **50**, 3067–3071 (2011).